MURI: Collaborative Research on Novel High Power Sources for the Physics of Ionospheric Modification

Sponsor: AFOSR - FA95501410019
1/09/15 Year1 report

Participating Universities:
Institute for Research in Electronics and Applied Physics (IREAP), University of Maryland
Space and Plasma Physics (SPP), University of Maryland
Texas Tech University
University of California, Los Angeles

Point of Contact: Prof. Thomas Antonsen
University of Maryland
Departments of Electrical and Computer Engineering and Physics and Institute for Research for Electronics and Applied Physics College Park, MD

DOD Points of Contact:
Dr. John Luginsland - AFOSR
Dr. Kent Miller - AFOSR

Introduction

The overall goals and objectives of this Multidisciplinary University Research Initiative are to develop prototypes of EM sources for mobile, reconfigurable ionospheric heaters based on:

(i) Comprehensive understanding of the current status of IM research and applications;

(ii) Combination of theoretical/modeling with laboratory experiments scaled to simulate ionospheric plasma parameters at different geo-magnetic latitudes and diurnal variation and solar cycle;

(iii) Understanding of modern high power RF source technology and antenna engineering including meta-materials.

Tasks are divided into two main areas along items (i), (ii) and (iii) above. The Space Plasma Physics Group of UMD and the Laboratory Space Experimental group of UCLA are focusing on items (i) and (ii), and the Charged Particle Beam Group of UMD and the Pulsed Power group of Texas Tech are focusing on item (iii). Within item (iii) Texas Tech is pursuing RF generation using laser triggered photoconductive switches (PCSS), and design of electrically small antennas. The UMD team is developing a high efficiency Inductive Output Tube (IOT). Progress in each area is described in what follows.

UMD-SPP Group - Progress

Experimental Studies of the Artificial Ionospheric Turbulence

Recent theoretical models predict that super small striations (SSS) of the electron density having ten centimeters size can be excited by HF waves with frequency close to multiples of the electron gyro frequency. We report the results of experiments conducted during the HAARP 2013-2014 campaigns, whose objective was to study the development of artificial ionospheric turbulence. During the experiments, the heating frequency was stepped up and down near the 4th gyroharmonic, and the power of the heating HF radiation was varied. Our diagnostics included: measurements of phase-derived Slant Total Electron Content using the L1/L2 signals from PRN 25 GPS satellite received at HAARP; measurements of Stimulated Electromagnetic Emission (SEE) conducted 15 km away from the HAARP site; detection of the HAARP HF radiation at Ukrainian Antarctic Station (UAS) located 15.6 Mm from HAARP; ionograms from HAARP's digisonde and reflectance data from Kodiak radar located 660 km South of HAARP.

Differential phase measurements of the GPS signals passing through the heated region in the presence of SSS with extremely high amplitude ($\delta n/n$=0.2-0.3)at scale size comparable to the electron gyroradius were detected. It was found that the highest amplitude of GPS scintillations coincides with the highest level of the Broad Upshifted Maximum (BUM) and occurs when the HF frequency is slightly above the fourth harmonic of the electron cyclotron frequency. Such irregularities affect UHF signals including GPS, and thus can be important in applications. Furthemore, frequency sweeps indicate that the scintillation amplitude exhibits hysteresis similar to that observed for the BUM amplitude when the HF frequency is cycled about the fourth harmonic of the cyclotron frequency.

Another experiment used HAARP signals detected at UAS as diagnostic for the artificial ionospheric turbulence. The observations showed: a distinct correlation between the broad upshifted maximum detected by the SEE and strong suppression of the HF signals detected at UAS station; drift velocity of the ionospheric irregularities causing HF scattering detected at UAS station corresponds to that measured by the Kodiak radar; the intensity of the scattered radar signals by Kodiak correlates with the amplitude of downshifted maximum observed by the SEE.

Our observations showed: a distinct correlation between the broad upshifted maximum detected by the SEE and strong suppression of the HF signals detected at UAS station; drift velocity of the ionospheric irregularities causing HF scattering detected at UAS station corresponds to that measured by the Kodiak radar; the intensity of the scattered radar signals by Kodiak correlates with the amplitude of downshifted maximum observed by the SEE. The analysis shows that origin of the detected signal at UAS is scattering of the HAARP's HF radiation off of artificially pumped striations and into the ionospheric waveguide.

Incidence angle dependence of Langmuir turbulence and artificial ionospheric layers driven by high-power HF-heating

In this work we continue our development of the theoretical model of descending artificially ionized layers in the ionosphere, which were discovered in 2010 by Pedersen et al. Our 2012 paper introduced the multi scale model of the discussed process. During the last year we have numerically investigated the development of strong Langmuir turbulence and associated electron acceleration at different angles of incidence of ordinary mode pump waves. For angles of incidence within the Spitze cone, the turbulence initially develops within the first maximum of the Airy pattern near the plasma resonance altitude. After a few milliseconds, the turbulent layer shifts downwards by about one kilometer. For injections outside the Spitze region, the turning point of the pump wave is at lower altitudes. Yet, an Airy-like pattern forms here, and the turbulence development is quite similar to that for injections within the Spitze. SLT leads to the acceleration of 10-20 eV electrons that ionize the neutral gas thereby creating artificial ionospheric layers. Our numerical modeling shows that most efficient electron acceleration and ionization occur at angles between the magnetic and geographic zenith, where SLT dominates over weak turbulence. Possible effects of the focusing of the electromagnetic beam on magnetic field-aligned density irregularities and the finite heating beam width at the magnetic zenith were also discussed.

2. Collaboration with outside groups

Naval Research Laboratory: Paul Bernhardt, Carl Siefring, Stan Bricinski
BAE Systems: Chia-lie Chang
Cornel University: Mark Psiaki, Karen Chiang
Institute of Radio Astronomy, National Academy of Sciences of Ukraine, Kharkov, Ukraine: Yuri Yampolski, Alex Koloskov, Alex Sopin, Andrei Zalizovski
University of Alaska, Fairbanks: Bill Bristow Virginia Polytechnic Institute: Mark Ruohoniemi.

3. Students and postdocs supported by the MURI

Alireza Mahmoudian (Postdoctoral Associate) Aram Vartanyan (PhD student) Chris Majmi (PhD student) Anand George (MSc student)
Karuna Karan (MSc student)

4. Journal Publications

A. Najmi, G. Milikh, J. Secan, K. Chiang, M. Psiaki, P. Bernhardt, S. Briczinski, C. Siefring, C.L. Chang, and K. Papadopoulos (2014), Generation and detection of super small striations by F-region HF-heating, J. Geophys. Res., 119, doi: 10.1002/2014JA020038.

5. Invited Presentations

D.Papadopoulos, A new paradigm in sources and physics of high-power ionospheric modidifications (invited review), 20th Annual RF Ionospheric Interactions workshop, April 2014, Arecibo, Puerto-Rico.

K.Papadopoulos, Upper hybrid effects in artificial ionization (invited talk), Fall AGU meeting, December 2014, San Francisco, California

B. Eliasson, G. Milikh, X. Shao, E.V. Mishin, and K. Papadopoulos (2014), Incidence angle dependence of Langmuir turbulence and artificial ionospheric layers driven by high-power HF-heating, *J. Plasma Phys*., doi:10.1017/S0022377814000968.

Space Physics

D. Papadopoulos, Ionospheric modifications using mobile, high power HF transmitters based on HPM technology (invited talk), ICOPS, May 2015, Belek, Antalya, Turkey.

6. Contributed Presentations

A.Najmi, G. Milikh, J. Secan, K. Chiang, M. Psiaki, P. Bernhardt, S. Briczinski, C. Siefring, C.L. Chang and K. Papadopoulos, Super Small Striations (SSS) and F-Region Heating at HAARP, 20th Annual RF Ionospheric Interactions workshop, April 2014, Arecibo, Puerto-Rico.

A.Vartanyan, G. Milikh, B. Eliasson, A. Najmi, M Parrot, K. Papadopoulos, VLF generation by continuous HF heating of the upper ionosphere, , 20th Annual RF Ionospheric Interactions workshop, April 2014, Arecibo, Puerto-Rico.

G. Milikh, Studies of the Ionospheric Turbulence Excited by the Fourth Gyroharmonic at HAARP, Fall AGU meeting, December 2014, San Francisco, CA.

A.Najmi, B. Ellison, X. Shao, G. Milikh, K. Papadopoulos, Vlasov simulations of ionospheric heating near the upper hybrid layer, Fall AGU meeting, December 2014, San Francisco, CA.

UCLA Experimental Program Progress

Experiments related to ionospheric modification using RF waves on the Large Plasma Device (LaPD) at UCLA have been focused on the generation of low frequency waves ($f \sim f_{ci}$) by modulated intense perpendicular propagating microwave pulses ($k \perp B_o$, $f \sim f_{ce}$). Initial results have demonstrated the generation of coherent shear Alfvén waves at any selected frequencies ($f < f_{ci}$) determined by the heating pulse spacing.

A MW solid-state modulator was designed and constructed at UCLA for this experiment. The modulator is capable of firing rapid consecutive high power energy pulses at tunable modulation frequencies ($\Delta\tau \sim 1$ μs, $f_{modulation}$ as high as 200 kHz). The pulses were converted into X-band microwaves near the upper-hybrid frequency and delivered into the plasma transverse to the background magnetic field parallel to the plasma density gradient. The electromagnetic energy was found to be deposited into a narrow plasma layer determined by the plasma density profile and the background magnetic field (fig 1).

The high power microwaves coupled to the plasma and generated super-thermal electrons and current channels. When the pulses were modulated at a frequency of a fraction (0.1-

1.0) of f_{ci} (ion cyclotron frequency), coherent magnetic field oscillations near this frequency were detected, and continued after the driving microwaves are turned off (Fig 2). The wave pattern radiated by this "virtual antenna" [1] was found to be very similar to that launched by a physical RMF (Rotating Magnetic Field) antenna [2] (Fig 3).

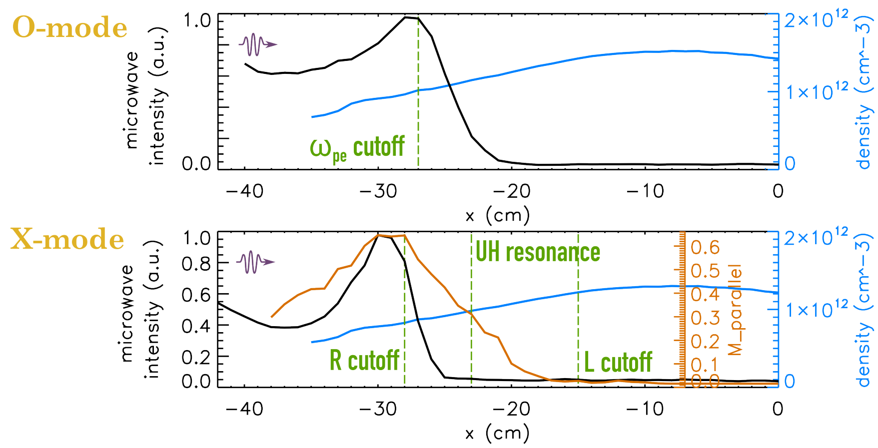

Fig 1. Experimental measurements of microwave intensity along the propagation direction (x-direction; the background magnetic field is in z-direction), black; plasma density profile, blue; parallel Mach number, orange. The microwaves were broadcast from outside the plasma on negative x-axis. They were polarized to O-mode (top) or X-mode (bottom). The location of cutoffs and resonance associated with these two modes are also marked, which are calculated from (n_e, B_0) independently measured in the experiment.

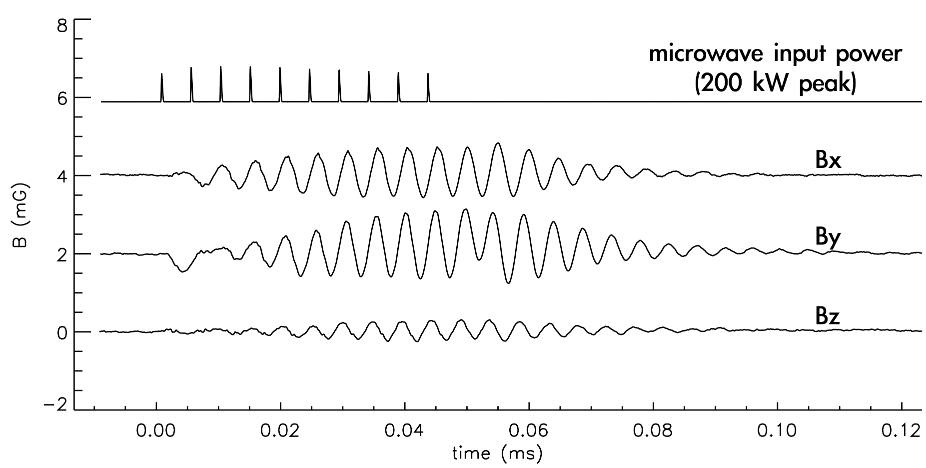

Fig 2. Input microwave power and the oscillating magnetic field measured by a magnetic pickup coil located at dz = 260 cm from the microwave source. The measured B field was nearly sinusoidal, indicating a narrow frequency band. Further spectrum analysis showed the peak frequency was the same as the driving frequency. The oscillating magnetic field was dominantly in the perpendicular direction (B_o is in z-direction).

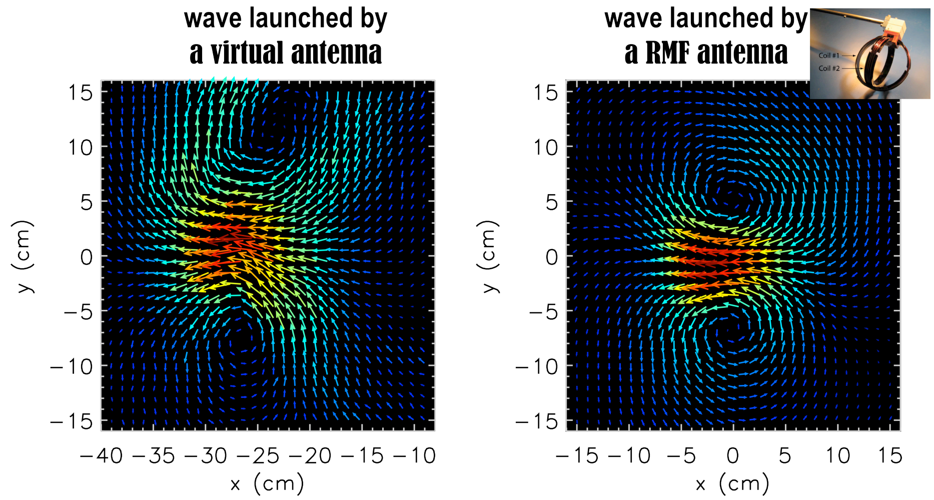

Fig 3. Measured $B_\perp$ vectors on a plane transverse to B_o, comparing wave generated by the virtual antenna, left, and that by a physical (Rotating Magnetic Field) antenna, right. Both measurements show similar patterns with two axial current channels in the opposite direction. In the case of the left panel, the high power microwave pulse heats electrons and creates a current channel centered about (x,y)=(-26,-4) cm, and the plasma responds to it by forming a return current.

To confirm these oscillations are shear Alfvén waves, the modulation frequency was varied between $0.24*f_{ci}$ and $1.05*f_{ci}$ while f_{ci} is fixed at 247 kHz. The magnetic components of the low frequency waves were measured on two transverse planes at axial distance of dz = 128 cm and dz = 224 cm away from the microwave source. The phase velocity of the wave was obtained by calculating correlation between the two measurements. The measurements agreed well with theoretical dispersion relation of shear Alfvén waves (Fig 4).

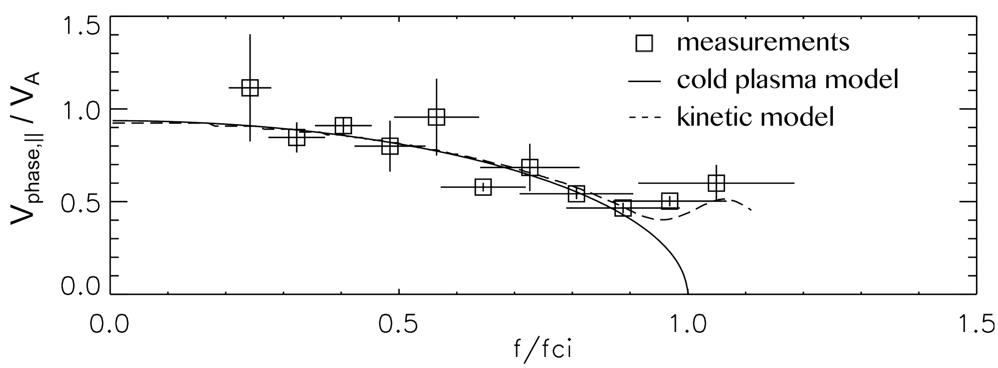

Fig 4. Measurements compared with the theoretical shear Alfvén wave dispersion relations. The measurements agree well with cold plasma dispersion relations below f_{ci}. The theoretical curve continues through f_{ci} when a finite ion temperature is included [3], as shown by the dashed line ($T_e = T_i = 2$ eV).

An analytic model, adapted and modified from [4], is in development to further guide the experiment. The model assumes each microwave pulse creates a localized current source and the total current is an impulse train in time

$$\vec{J}_{ext}(\vec{r},t) = \sum_{n=0}^{N-1} J_0 \delta(t-n\Delta T)\delta(z)\exp(-r^2/d^2)\hat{z},$$

then the magnetic field oscillation in the uniform cold plasma due to the imposed source is given by

$$\vec{B}(\vec{r},t) = \frac{J_0 d\delta_e}{\sqrt{2}\pi}\int_0^{k_{max}} dk_\perp \int_0^{\omega_{max}} d\omega \frac{\omega^2 k_\perp^2}{v_A^2(1-\omega^2/\omega_{ci}^2)} \exp(-k_\perp^2 d^2/4) J_1(k_\perp r) h(z,t,k_\perp,\omega),$$

where $h(z,t,k_\perp,\omega) = \frac{1}{k_A}\sum_{n=0}^{N-1}\sin(k_A z-\omega t+n\Delta T)H(-k_A z+\omega t-n\Delta T)$ and $H(x)$ is the step function, $k_A^2 = \frac{\omega^2(1+k_\perp^2\delta_e^2)}{v_A^2(1-\omega^2/\omega_{ci}^2)}$, $v_A^2 = c^2\omega_{ci}^2/\omega_{pi}^2$, $\delta_e = c/\omega_{pe}$, $k_{max} = \frac{1}{\delta_e}\sqrt{\frac{v_A^2 t^2}{z^2}(1-\omega^2/\omega_{ci}^2)-1}$, $\omega_{max} = \omega_{ci}\sqrt{1-(1+k_\perp^2\delta_e^2)z^2/v_A^2 t^2}$, and $J_1(r)$ is the Bessel function of the first kind for order 1. The calculation has shown higher efficiency of Alfvén wave generation for modulation frequencies above $f_{ci}/2$ then that of below $f_{ci}/2$, which is in accord with the results from the preliminary experiment.

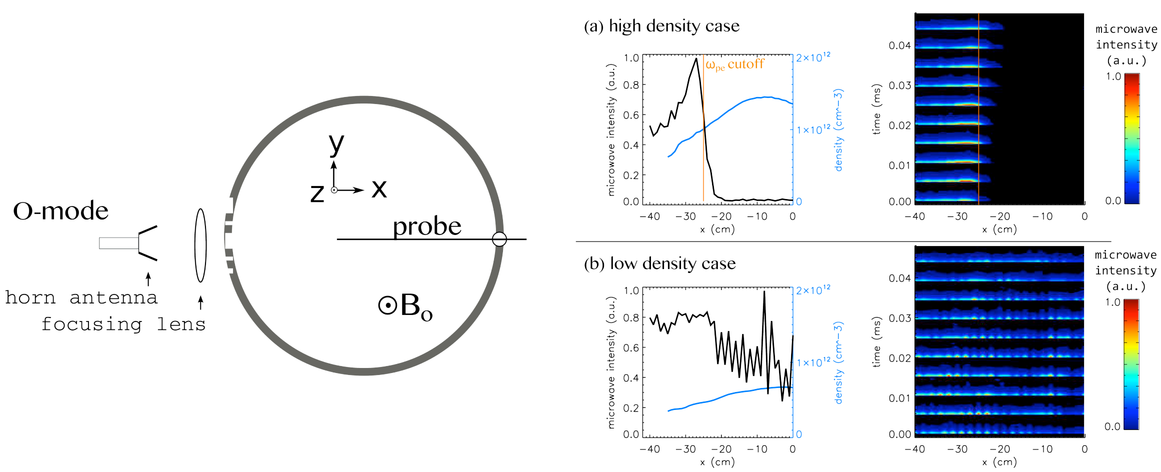

Fig 5. In the case of a dense plasma ($w_{microwaves}/nkT_e \approx 1$, top panel) the microwave intensity distribution was fairly smooth until the beam hit the cutoff layer. However, in the low-density case (bottom panel) where the relative microwave power density was higher ($w_{microwaves}/nkT_e \approx 10^2$), the microwaves seemed to be concentrated in very narrow channels.

Additional information will be gathered in the coming experiments to complete this work. As examples, planned experiments include: measurement of the energy distribution of the fast electrons generated by the microwave, the Alfven wave spectrum evolution as function of the number of microwave pulses, and the partitioning of the incident microwave energy between bulk plasma heating, plasma flow, radiated energy and reflected microwaves out of the plasma.Besides the virtual antenna experiment, we are also planning experiments on the micro-physics of coupling of the high power microwaves with the plasmas. One example is the formation of field-aligned filaments in presence of these high power microwaves. Possible evidence of such filaments at very low plasma density was recorded in the preliminary experiment (Fig 5). In the coming experiments we will do a more detailed study on this subject.

Roadblocks:

The biggest roadblock on the experimental side is insufficient funds for what is planned in the future. We must build a 3D computer controlled probe drive system with sub-millimeter resolution to resolve the expected filaments. In addition the laboratory needs to purchase X band diagnostics components (mixers, amplifiers, filters, high frequency low loss coaxial cables). High frequency probes must be constructed to diagnose waves in the vicinity of the absorption layer. The project would also greatly benefit if there were funds for a graduate student.

1) Graduates students involved : none
2) Postdoctoral Research Scientist : Yuhou Wang
3) Publications: none so far. There will be a publication this year
4) Conference Proceedings: Wang, Y., Gekelman, W., Pribyl, P., Van Compernolle, B., Papadopoulos, K. , "Exciting Alfven Waves using Modulated Electron Heating by High Power Microwaves", *Bull. APS-DPP*, *136 (2014)*

[1] K. Papadopoulos, et al., Geophys. Res. Lett. 38, 2011
[2] Gigliotti, et al., Phys. of Plasmas 16.9, 2009: 092106; Karavaev, et al., Phys. Plasmas 17.1, 2010: 012102.
[3] S. Vincena, et al., Phys. Plasmas, v8, n9, 3884, 2001.
[4] B. Van Compernolle, et al., Phys. Plasmas, v15 082101, 2008.

Source and Antenna Development Development

Texas Tech Pulsed Power Group Progress

Researchers at Texas Tech have addressed the areas: Electrically small antennas, photoconductive switching, PCSS, for high average power rf generation, and micro discharges as pulsed light sources for PCSS triggering

An electrically small antenna design, see Fig. 6, has been extensively studied to potentially be used in an Ionospheric heating array. The frequency range of the antenna has been the primary source of interest, since the array is meant to match the operation of HAARP, with a range of 2.8 to 10 MHz. Since the antenna size scales with wavelength, the antennas that were studied were designed for the 28 to 100 MHz range and were one tenth of the size to cut down fabrication costs in this early stage. It was found that inserting a dielectric between the capacitive stubs of the antenna provided an elegant means of tuning the antenna. The simulated relationship between the amount of dielectric inserted and the operating frequency of the antenna is shown in Figure 7. Unfortunately, there are several antenna performance aspects that decrease as the antenna's operating frequency is decreased, most importantly the instantaneous bandwidth, the radiation efficiency, and the gain. To verify the simulations, an antenna was built, and preliminary testing shows that inserting a dielectric is a valid way to tune the antenna.

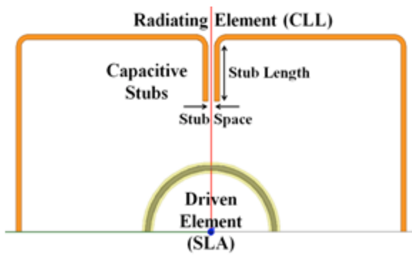

(a)

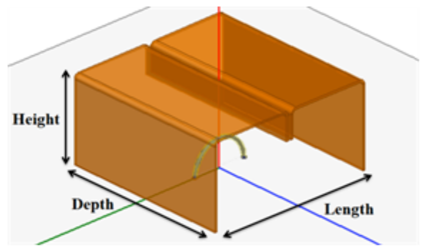

(b)

Fig 6. (a) A cross-sectional view of the antenna is shown, with the major components labeled. (b) The three-dimensional antenna is shown from an upward angle

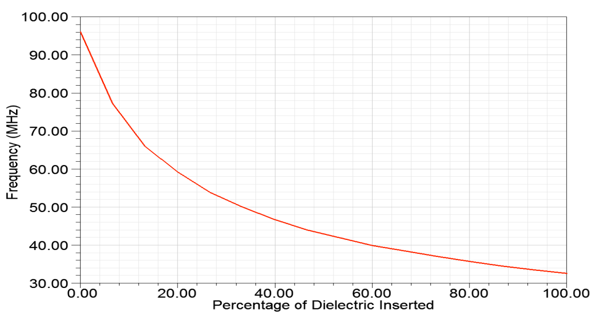

Fig. 7 In simulation, the dielectric was moved through the entire 30 cm length of the capacitive stubs at 2 cm intervals. The operating frequency was evaluated as the frequency at which the reflection from the antenna was minimized.

The antenna drive impedance is matched to 50 Ohm such that the antenna may be fed by any standard rf tube or the new tube developed at UMD.

Regarding development of a solid state driver for the ionosphere heater (IH), significant progress has been made in uncovering the degradation mechanisms limiting the lifetime of the photoconductive semiconductor switches (PCSSs). These switches have previously demonstrated the ability to produce high output powers (>10 MW) at frequencies ranging from 50 MHz – 400 MHz. However, these devices have demonstrated limited lifetime in the form of cracks forming in the semiconductor material near the metal/semiconductor interface, see Fig. 8 for an example.

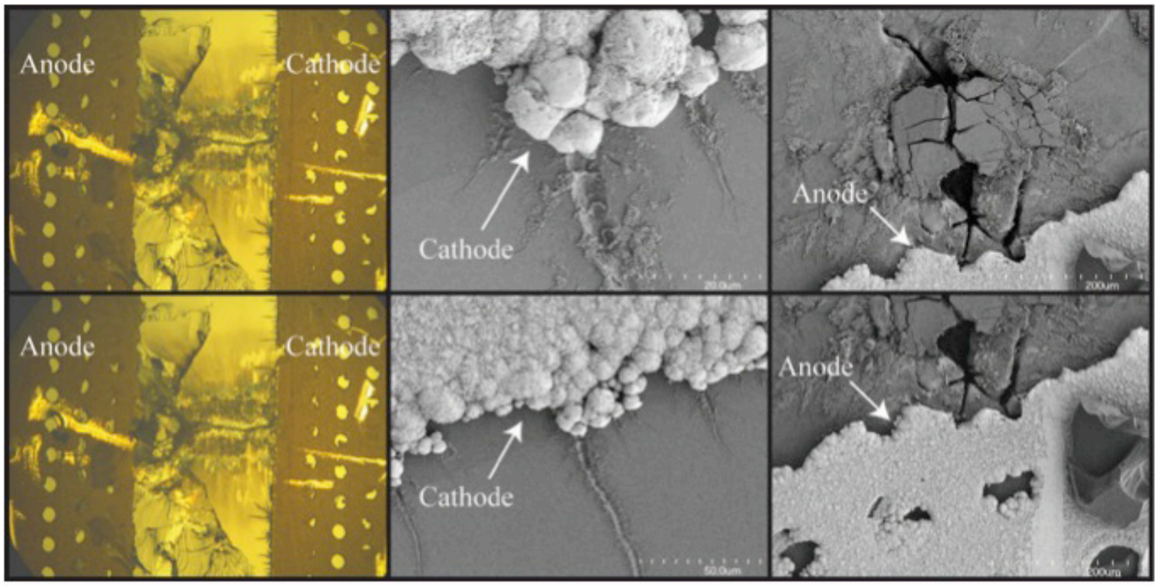

Fig. 8 Optical (left) and SEM (center and right) images of a failed SiC PCSS.

Two hypotheses were evaluated concerning the root-cause of these cracks. The first hypothesis was that high current densities near the metal semiconductor interface were the cause of the cracking. The second was that transient electric fields during the switch closing and opening were the cause of the cracks. Both simulation and experimental results strongly suggest that transient electric field during switch closing and opening caused by the spatial and temporal distribution of the gating laser pulse is the root-cause of the cracks. That is, a 2D finite difference time domain code was implemented using MATLAB as programming platform, see Fig. 9.

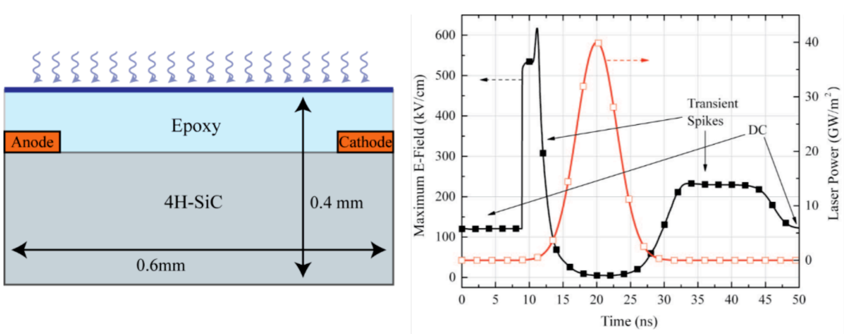

Fig. 9 Left - simulation domain. Right - Simulation results (maximum electric field versus time and laser pulse versus time).

The code uses a quasi- electrostatic approach to capture in first order the electric fields seen by the PCSS during switch closing and opening. In order to experimentally test the transient electric field hypothesis, the test-setup was modified in order to collapse the electric field across the device before the end of the gating laser pulse. Hence, the electric field is not present during switch opening, which then resulted in significantly fewer cracks than the PCSS switched compared to the original test setup. Subsequently, future plans include modifying the spatial distribution of the incident light in order to confirm this theory. The development of a high power, microdischarge (MD) based, repetitive light source to trigger SiC photoconductive switches is currently underway. Such a light source will complement existing high power laser sources, enabling a wide range of pulse widths and pulse repetition rates up to 10+ MHz. Building on previous work, current studies have been focused on a 121.6 nm vacuum UV (VUV) source. Fundamental characterization of the microdischarge using Stark broadening was completed, to indicate the operation mode of the microdischarge, see Fig. 10.

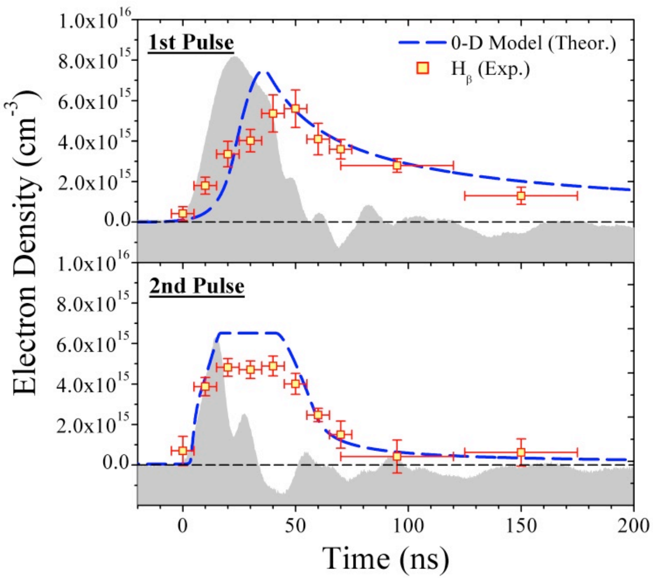

Fig. 10 Temporal electron density dynamics in a 1 MHz rep-rated microdischarge. Relative applied voltage level is indicated by gray shaded region.

The study of the influence of pulse width and pulse repetition rates on MD light source behavior, detailing peak and average power, efficiency, and impurity content was also completed. Figure 6 shows a portion of these results where peak VUV power under various pulse repetition rates and widths is graphed. In this study, it was observed that lower pulse repetition rates typically provided more favorable performance (i.e. higher efficiency and peak power) for this specific geometry and gas mixture.

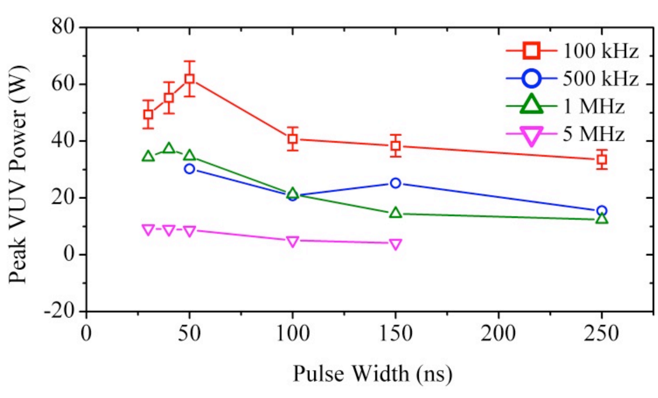

Fig.11 Peak VUV power of a microdischarge versus pulse width for various pulse repetition rates.

For the production of UV light, $XeCl^*$ (308 nm) and XeF^* (351 nm) excimer sources will be used. Due to the corrosive and toxic nature of these gases, a completely new MD system had to be implemented. Much of the new experimental setup has been fabricated and is ready for use. Current tasks include nickel-plating the MD to avoid corrosion during operation and basic MD light source characterization.

Personnel supported

Students

Daniel Mauch, Paul Gatewood, John Shaver, Jacob Stephens, David Thomas, Shannon Feathers

Faculty

Andreas Neuber, John Mankowski, James Dickens

Staff

Earl Waldrep, Kathryn Flanagan

Publications

Journals

- D. Mauch, D., W. Sullivan III, A. Bullick, A. Neuber, and J. Dickens, "High Power Lateral Silicon Carbide Photoconductive Semiconductor Switches and Investigation of Degradation Mechanisms." IEEE Transactions on Plasma Science. Under review.

- D. Mauch, C. Hettler, W. Sullivan III, A. Neuber, J. Dickens, „Evaluation of a Pulsed Ultra-Violet Light-Emitting Diode for Triggering Photoconductive Semiconductor Switches," IEEE Transactions on Plasma Science. Under review.

- J. Stephens, A. Fierro, B. Walls, J. Dickens, A. Neuber, "Nanosecond, repetitively pulsed microdischarge vacuum ultraviolet source" Applied Physics Letters 109, 074105 (2014).

- J. Stephens, A. Fierro, J. Dickens, A. Neuber, "Temporally resolved electron density of a repetitive, nanosecond pulsed microdischarge" Journal of Physics D: Applied Physics 47, 465205 (4pp) (2014).

- J. Stephens, A. Fierro, D. Trienekens, J. Dickens, and A. Neuber, "Optimizing drive parameters of a nanosecond, repetitively pulsed microdischarge high power 121.6 nm source," Plasma Sources Science and Technology 24, 015013 (6pp) (2015).

Conference proceedings

- (*Invited* Oral Presentation and Authored Manuscript for the 2014 IEEE International Power Modulator and High Voltage Conference) Mauch, D., C. White, D. Thomas, A. Neuber, and J. Dickens, "Overview of High Voltage 4H-SiC Photoconductive Semiconductor Switch Efforts at Texas Tech University." Presented at the 2014 IEEE International Power Modulation and High Voltage Conference. To be published.

- P. Gatewood, A. Neuber, J. Dickens, and J. Mankowski, "A Metamaterial-Inspired Electrically Small Antenna for Operation at 2 to 20 MHz," presented at IEEE IPMHVC 2014 (to be published).

- D. Thomas, D. Mauch, C. White, A. Neuber, J. Dickens, "Characterization of Mid-Bandgap Defect States in Silicon Carbide Through Leakage Current Analysis for Optimization of Silicon Carbide Photoconductive Semiconductor Switches, " presented at the International Power Modulator and High Voltage Conference, Santa Fe, NM, June 2014.

Collaborations / Visits:

- Ongoing discussions with Ness Engineering, nessengr@san.rr.com, regarding expansion of SiC switch technology to GaN. Collaboration on STTR.

- Visit by John Blevins, AFRL Sensors directorate DR-03 USAF AFMC AFRL/RYDD, john.blevins.2@us.af.mil, to discuss PCSS technology and applications in their directorate.

- Visit by Dr. John Metzger, Kyma Technologies, metzger@kymatech.com, exploring future funding opportunities on PCSS switching. Kyma is one of the few seminsulating GaN (the kind that is needed for optically triggered PCSS switching) manufacturers in the US. Received GaN samples free of charge for material testing.

UMD Charged Particle Beam Group Progress

The effort here is to develop a high efficiency Inductive output tube (IOT) that operates in the frequency range 2 – 10 MHz. To increase efficiency class D operation in which the beam is on during only a portion of the RF cycle is considered. Efforts were focused on study of beam modulation in high power guns. The plan was to measure and simulate class D operation to gain experience and confidence in the simulation codes. While progress was made in simulation, the experimental effort was set back by the failure of several guns that were available in IREAP. We are currently pursuing a collaboration with the Naval Research Lab, which has two IOT guns. Our hope is to both measure and simulate the operation of these guns in class D mode. Preliminary measurements have been made. We are now waiting for completion of a Nondisclosure Agreement between UMD and CPI, the manufacturer of the guns, which will us access to the internal dimensions of the gun so that we may simulate it.

A second experimental effort was directed at studying the possibility of using a ferrite to electrical tune the output cavity. A series of measurement were made. The conclusion was that although the ferrite could vary the resonant frequency of a cavity over the desired range, the losses in the ferrite would be excessive, and negate the high efficiency benefits of operating in class D mode. We are now looking at the possibility of designing an output circuit in which the capacitance is mechanically varied to allow coverage of the desired frequency range. Initial calculations are encouraging in that it appears to be possible with an over-coupled transformer to maintain constant impedance at the decelerating gap, while varying the resonant frequency of the circuit.

Simulations focused on development of a Magnetron Injection Gun configuration in which the need for a semi transparent grid is eliminated, and simulation of beam deceleration in the output gap of a device. These will be described below.

Magnetron Injection Gun (MIG) IOT Simulations

A. Steady State Simulations

One of the major concerns with the gridded 'Class D' operation of an IOT device is the heating of the grid due to intercepted electrons. A design using a MIG-type cathode that produces a hollow beam avoids this complication, as a small mod-anode local to the thin annular cathode can be used to bias the beam on and off without intercepting any electrons. We already possess a MIG-type cathode that could be useful for this purpose. The proposed source with a Pierce-type geometry has been characterized with the Michelle code [5] with 2D axisymmetric geometry as shown in Fig. 12. Steady state electrostatic PIC simulations show that for 60 kV on the anode and 200 V on the mod-anode, we can expect 2 Amps output current.

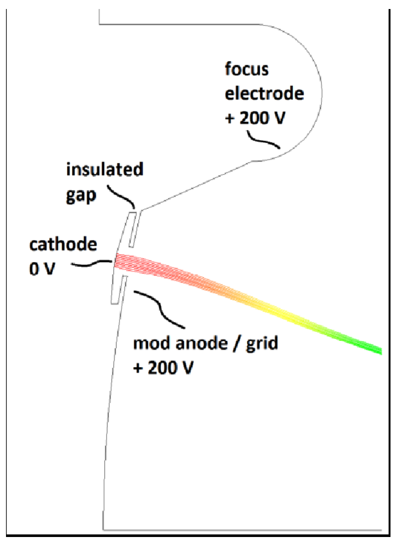

Fig 12 Geometry of cathode, focusing electrode and mod-anode of a MIG-type gun. Particle traces shown in color.

The magnetic field design was identified by using Maxwell 2D (axisymmetric geometry) to simulate solenoid coils/pole piece geometries. Iterations over several geometries maximized the dot product of the field lines with the unmagnetized beam trajectory (to minimize conversion of longitudinal to transverse momentum). The most recent iteration is shown below in Fig. 13. The field lines follow the unmagnetized beam trajectory closely, except near the cathode surface. An additional set of coils or iron field shapers behind the cathode may be used to adjust the field lines in this region. As seen in simulation (Fig. 15b), with a 1.4 kGauss field, the beam ripple due to transverse energy gain is minimal. This field simulation assumes ideal iron.

Steady state Michelle simulations were used to estimate the capacitance seen by the grid driver due to the focus electrode-mod anode spacing in the vicinity of the cathode. Calculations were done with and without beam in a 2D axisymmetric Michelle simulation, and the no-beam case was verified against a Maxwell 3D model of the gun assembly. Michelle and Maxwell measurements agreed to within 2%, with the most likely discrepancy being a difference in mesh density. Additionally, comparison of

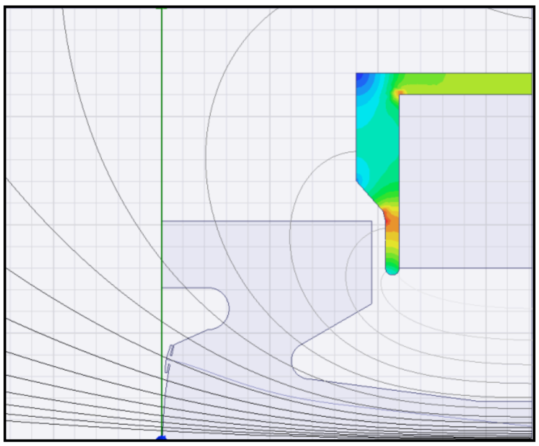

Fig. 13: Maxwell 2D simulation, flux lines from iron pole piece and copper coils overlaying sketch of MIG source.

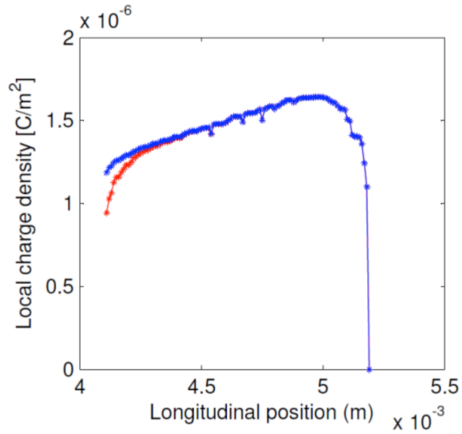

Fig. 14: Charge on inner mod-anode surface with (blue) and without (red) beam.

Michelle simulations with and without beam predicts a 1% increase in capacitance due to beam loading (Figure 3). We predict that the capacitance due to the inner surface of the mod-anode is 15.6 pF, requiring the grid driver to pull 2 A for a 5 ns rise time on a 600 V swing. However, this estimate does not account for capacitance in the transfer line, which may be considerable.

B. Time domain simulations

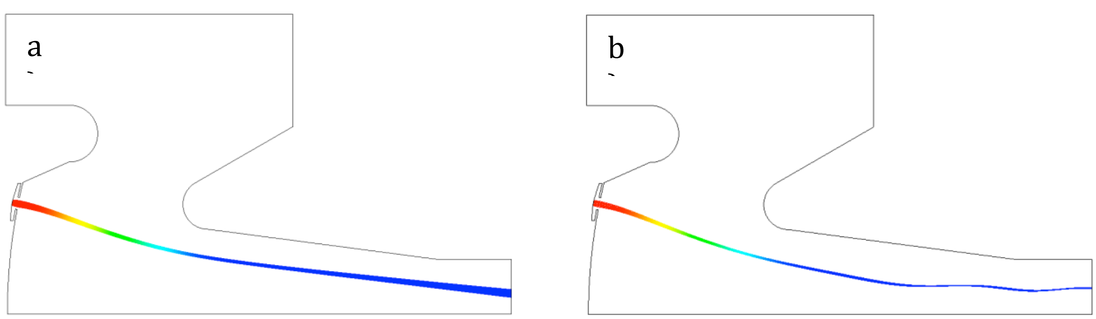

Fig. 15: (a) Unmagnetized beam trajectory (color corresponds to beam energy). (b) Beam trajectory with field from Fig. 2, peak on-axis field of 1.4 kGauss.

We have used the Michelle electrostatic time domain solver to probe MIG IOT performance with pulsed grid voltage. The cathode-grid IV curve is constructed by allowing the grid voltage to slowly ramp (12 V/ns) at fixed anode voltage 60 kV, as shown in Figure 5a. The perveance in the cathode-mod anode gap is fitted to be 17.7 micro-Pervs, and the turn-on voltage is at -308 V. A 5 MHz square wave-pulse with

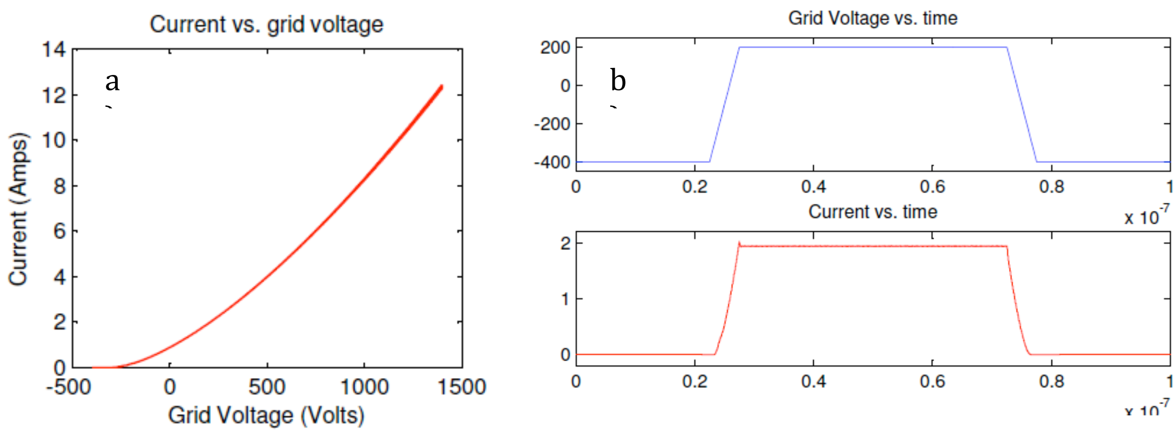

Fig. 16 (a) IV curve for mod-anode voltage, at fixed (60 kV) anode. (b) Square wave pulse and output current for modulated MIG source.

voltage swing -400 to +200 V and 5 ns rise and fall time and 0.25 duty factor, parameters comparable to the proposed class D operation, was passed to the Michelle simulation. One cycle of the output current is shown below, in Figure 16b.

Preliminary Simulation of Reflected Particles in Output Cavity

A preliminary series of axisymmetric electrostatic WARP [6] PIC simulations has been conducted to examine beam behavior resulting from application of a decelerating voltage that is a large fraction of the beam energy. The practical limits on the retarding voltage are an important factor limiting IOT efficiency. It is therefore desirable to approach these limits without generating reflected particles capable of intercepting the device walls and limiting device lifetime.

The configuration examined here is a standard Pierce gun diode with a 0.25 inch radius cupped cathode structure, operating at 37 KV and the nominal 3.28A space-charge-limited current. A 7mm wide 35KV retarding gap in the ~5cm (0.2in) radius wall is inserted 32mm downstream from cathode. Figure 6a is an x-z configuration space particle plot after 5ns, compared to a transit time of approximately 1ns. Also plotted on the same axes are equipotential contours and the location of conductor surfaces. In the case shown, the retarding voltage is just a few hundred volts above the limit at which no particles are reflected.

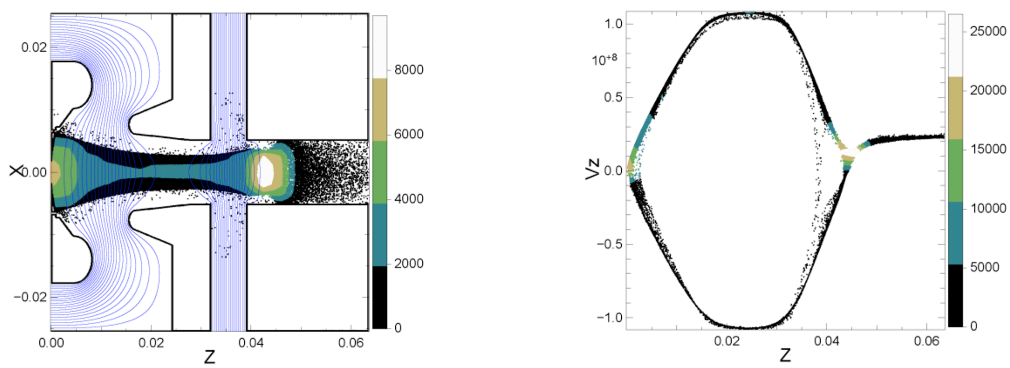

(a) (b)

Fig. 17: Particle plot (a) of x-z configuration space and equipotential contours for a 3.28A electron beam accelerated to 37KeV and then decelerated by 35.5KV, which is a few hundred volts above the threshold for reflecting particles. Beam is shown after 5ns, compared to the ~1ns transit time. Note that the combination of space-charge pileup and gap fringe-field defocusing drive an expansion of the beam radius downstream of the gap resulting in spreading the bulk of the beam into the beam pipe. (b) is a Vz-z phase space plot from the same simulation.

From Fig. 17a it is evident that a population of the reflected particles is outside the main beam body and that these particle can hit the conducting surface. As can be seen from Fig. 17b, some of these particles can acquire significant energy as they traverse the decelerating gap in the negative direction. By hitting the conductive wall these particles can have adverse consequences to the device lifetime. A standard technique to mitigate the dispersal of reflected particles outside the beam body is to immerse the beam in a longitudinal magnetic field. However, imposing a strong constant longitudinal field will maintain the beam at a constant beam radius. Because the cathode radius is greater than the anode aperture radius, this has the undesired result that the outer portions of the beam intercept the anode conductor. The anode geometry was therefore modified by simply increasing the radius of the anode aperture from 0.2in to 0.3in. In this way, particles that are emitted from the edges of the cathode and guided by the magnetic field, that travel at a near constant radius, will remain inside the radius of the anode aperture.

This modified geometry is shown in the z-x particle plot in Fig. 18a. The beam is guided by a 0.3T constant longitudinal field. This design is not optimal in the sense that the beam exhibits the launching of reflected particles at a lower retardation voltage than previously, so that the case shown in Fig. 18 is for a retardation voltage of 35KV compared to the 35.5KV in Figs. 17a and 17b. Some of this may be due to the modified geometry and some due to inward electrostatic focusing in the cathode anode region imparting transverse energy to the beam. Note the absence of any reflected particles outside the beam body. The population of reflected particles is clearly evident in Fig 18b, whch is a Vz-z phase space plot of the same simulation.
It can be seen in the Fig. 18b x-z configuration-space plot that the guiding magnetic field has surpressed any reflected particle from travelling outside the main beam body. This means that any reflected particles are decellerated as they travel through the anode-cathode region and, if intercepted, will have low energy.

Finally note that this work is only intended as a preliminary exercise to get ideas for areas appropriate for further study, especially since the studied geometry is likely to be quite different from the geometry that is ultimately adopted. Additionally, some of the conclusions may be modified when the full time-dependence of the control electrode and the actual retarding field are included.

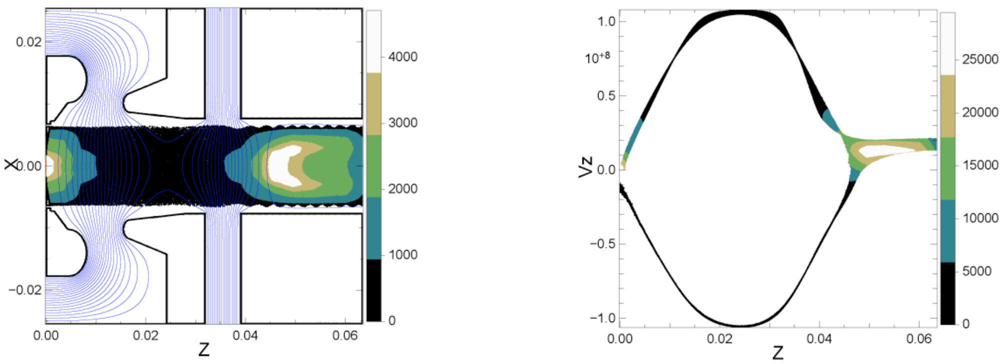

(a) (b)

Fig 18: (a) Configuration space plot of beam with 0.3T guide field. Geometry is modified so that anode aperture radius is greater than cathode. (b) Vz-z phase space plot showing the development of a population of particles reflected downstream of the decelerating gap.

Limiting current of an electron beam passing through a gap in a pipe

The development of high current accelerators in the late 1960's-early 1970's initiated an active study of limiting currents of charged particle beams that can be transported through metallic pipes in vacuum and/or plasma (see, for example, textbooks [7-9]) and references therein. The simplest case which allows for an analytical study of limitations due to the space charge effects is the case when a beam of charged particles (electrons or ions) propagates being guided by an infinitely strong external focusing magnetic field through a uniform metallic pipe. Below we study just such propagation in the presence of a gap in a pipe.

Consider a system schematically shown in Fig. 19. Here a cylindrical electron beam of an arbitrary cross-section (pencil-like or an annular one) propagates through a pipe being guided by an infinitely strong guiding magnetic field; so electrons perform a 1D motion in z-direction.

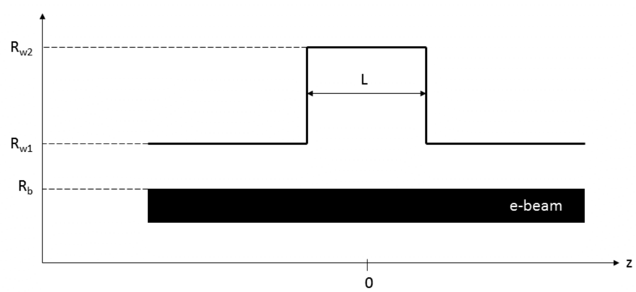

Fig. 19: Geometry of a beam propagating in a pipe with a gap

In the case of propagation in the uniform pipe, the limiting current can be found for the 1D Laplace equation for the potential

$$\frac{\partial}{\partial r}\left(r\frac{\partial \Phi}{\partial r} \right) = 0 \tag{1}$$

with the boundary conditions at the grounded wall $\Phi\left(R_w\right) = 0$ and at the outer surface of a beam having the outer radius

$$\left.\frac{\partial \Phi}{\partial r}\right|_{R_b} = \frac{2I_b}{R_b v}. \tag{2}$$

Eq. (2) follows from the Poisson equation. By using (1) and (2) one can readily find that the potential at the outer boundary of the beam is equal to

$$\Phi\left(R_b\right) = 2\frac{I_b}{v}\ln\left(\frac{R_w}{R_b}\right). \tag{3}$$

The most important detail of Equations (2) and (3) is the presence of the electron velocity in the denominator. This velocity depends on the potential since the electron energy normalized to the rest energy is

$$\gamma = \frac{1}{\sqrt{1-\beta^2}} = 1 + \frac{e}{mc^2}\left(V - \Phi\right). \tag{4}$$

In (4), $\beta = v/c$ is the velocity normalized to the speed of light, V is the accelerating voltage applied between the cathode and the anode. Thus, Equations (2)-(4) represent a set of nonlinear equations. The analysis of these equations carried out elsewhere [3-5] reveals that the maximum potential at which the solution of this set of equation exists is determined by the electron energy in the absence of space charge effects $\gamma_0 = 1 + eV/mc^2$:

$$\hat{\Phi}_{\max} = \gamma_0 - \gamma_0^{1/3}. \tag{5}$$

In (5) we introduced the normalized potential $\hat{\Phi} = e\Phi/mc^2$. The corresponding limiting current is equal to

$$I_{\max} = \frac{mc^3}{e}\frac{\left(\gamma_0^{2/3} - 1\right)^{3/2}}{2\ln\left(R_w/R_b\right)}. \tag{6}$$

Let us emphasize that Eq. (5) is valid for any cross-section of cylindrical electron beams.

After repeating this known result let us start analyzing a system with a gap shown in Fig. 8. Assume that the width of the gap L is on the order of the pipe radius R_{w1} and both are much smaller than the gap radius R_{w2}. Then, the potential in the gap region can be approximated by a simple formula

$$\Phi = \cos\left(\pi\frac{z}{L}\right)\left[\frac{K_0\left(\kappa r\right)}{K_0\left(\kappa R_{w2}\right)} - 1\right]. \tag{7}$$

In (7), $K_0\left(\kappa r\right)$ is the modified Bessel function of the zero order. At the wall $\Phi\left(R_{w2}\right) = 0$. Since we consider an electrostatic field, the absolute value of the transverse wavenumber κ in its argument of Bessel functions in (7) is equal to the axial number:

$$\kappa = \left| k_\perp \right| = \frac{\pi}{L}. \tag{8}$$

The strongest effect of the space charge field on the beam propagation takes place in the mid-plane z=0 where, as follows from (7) and (2),

$$R_b \frac{\partial \hat{\Phi}}{\partial r}\bigg|_{r=R_b, z=0} = -\kappa R_b \frac{K_1(\kappa R_b)}{K_0(\kappa R_b)} \hat{\Phi}(R_b) = -\frac{2}{\beta} \frac{eI_b}{mc^3}. \tag{9}$$

As follows from (9) and (5), the limiting current of this model $\hat{I}_{\max} = eI_{\max} / mc^3$ is equal to

$$\hat{I}_{\max} = \hat{R}_b \frac{K_1(\hat{R}_b)}{K_0(\hat{R}_b)} \frac{\left(\gamma_0^{2/3} - 1\right)^{3/2}}{2}. \tag{10}$$

In (10), $\hat{R}_b = \kappa R_b = \pi(R_b / L)$. At low voltages ($\hat{V} = eV / mc^2 << 1$) Eq. (10) reduces to

$$\hat{I}_{\max} \simeq \frac{1}{3}\sqrt{\frac{2}{3}} \hat{R}_b \frac{K_1(\hat{R}_b)}{K_0(\hat{R}_b)} (\hat{V})^{3/2}. \tag{11}$$

It should be noted that in this simplified model all geometrical factors are described by one combination $\Psi = \hat{R}_b K_1(\hat{R}_b) / K_0(\hat{R}_b)$ that depends on one parameter $\hat{R}_b = \pi(R_b / L)$ only.

The function $\Psi(\hat{R}_b)$ is shown in Fig. 20. In the case of large values of the normalized radius the function $\Psi(\hat{R}_b)$ can be approximated by

$$\Psi(\hat{R}_b) \simeq \hat{R}_b \frac{8\hat{R}_b + 3}{8\hat{R}_b - 1}. \tag{12}$$

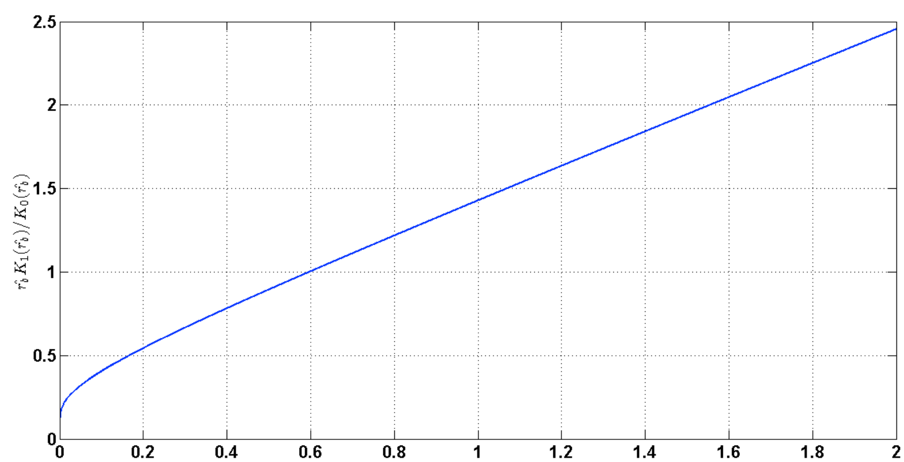

Fig. 20: Radial dependence of the limiting current in a pipe with a gap.

The PIC simulations of reflected particles in a gap for a 3.28A 37KeV beam illustrated that with a retarding potential of 35KV at the gap, particles are reflected (shown in Fig. 17b). The limiting current dependence on the beam voltage is shown below in Fig. 21.

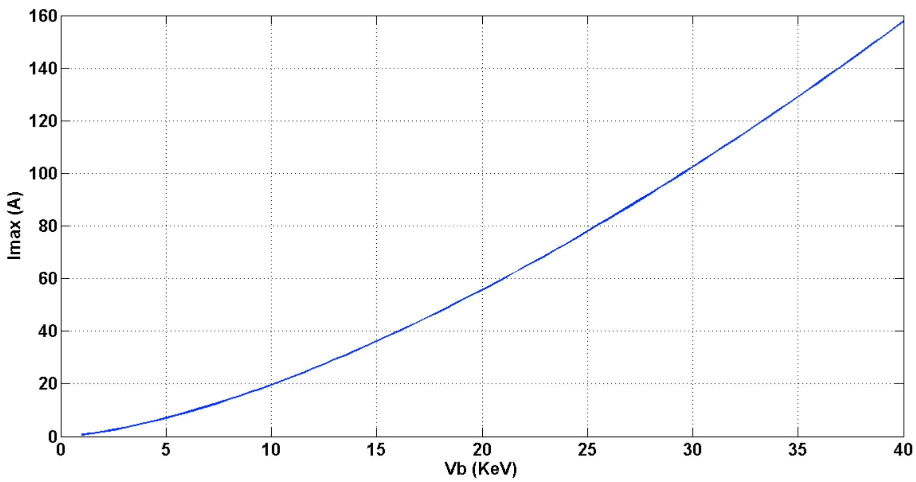

Fig. 21: Limiting current dependence on beam voltage

Compact Tunable Hybrid Cavity

The initial approach for the tunable cavity was to use a ferrite loaded structure as shown in Fig. 22a simulated using High Frequency Structure Simulator (HFSS) [6] an electromagnetic field solver typically used to model RF passive devices in a wide frequency range. This cavity design would allow us to easily tune electronically the resonant cavity across the entire frequency span of interest. The cavity design is shown in Fig. 22a and the tunable range versus the DC biased ferrite (or relative permeability) is shown in Fig. 22b.

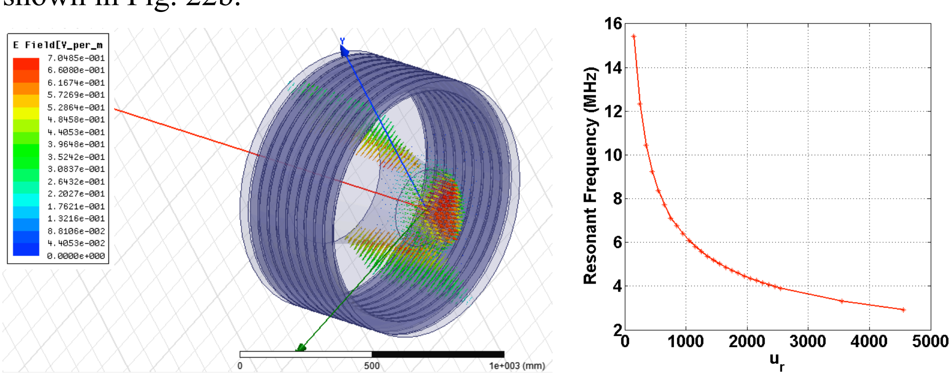

(a) (b)

Fig. 22a-b: (a) – Ferrite loaded resonant structure modeled in HFSS. (b) – Resonant frequency of the structure versus relative permeability (or DC bias).

When including the real loss tangent data from vendors, the ferrite loaded cavity was shown to be extremely lossy in the simulations, reducing the "Q"-Quality Factor to as low as 2. We also experimentally explored increasing the quality factor of ferrite loaded resonant structures by perpendicularly biasing the ferrites [11]. This was shown to work at TRUIMF and Fermilab boosters in the 50MHz region [10]. A prototype ferrite loaded structure was constructed and shown to not be successful as the magnetic loss tangent did not decrease sufficiently with bias fields upward of 1.1kGauss. We are now exploring copper ‘tank’ style resonant circuits similar to that found in AM broadcast transmitters (shown in Fig. 23a).

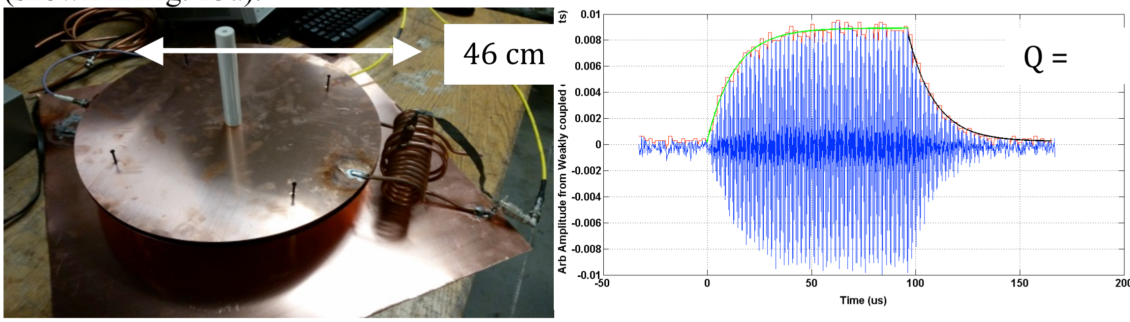

(a) (b)

Fig. 23a-b: (a) – Prototyping copper resonant structure at 7.23 MHz. (b) – Pickup probe measuring the natural Q during ‘ring-up and ring-down’ of the resonant structure in burst mode operation.

The next steps are to explore both input and output coupling of the prototype resonant structure. A weakly coupled pickup probe was placed near the structure to measure the natural Q (shown in Fig. 23b) of the circuit during burst mode operation, obtaining the ‘ring-up and ring-down’. The measured Q was 300.4 and the calculated Q was 305.5 assuming an AC resistance of 0.6W for the inductor.

Grid Driver in Class-D Amplifier Mode

The Michelle simulations of the gun indicate that the Magnetron Injection Gun (MIG) voltages required to bring the gun from cutoff to saturation are approximately 600-$700v_{pp}$. The modulator will drive the grid in burst mode at 1-10MHz with pulse widths of 50-150ns at low repetition rates.

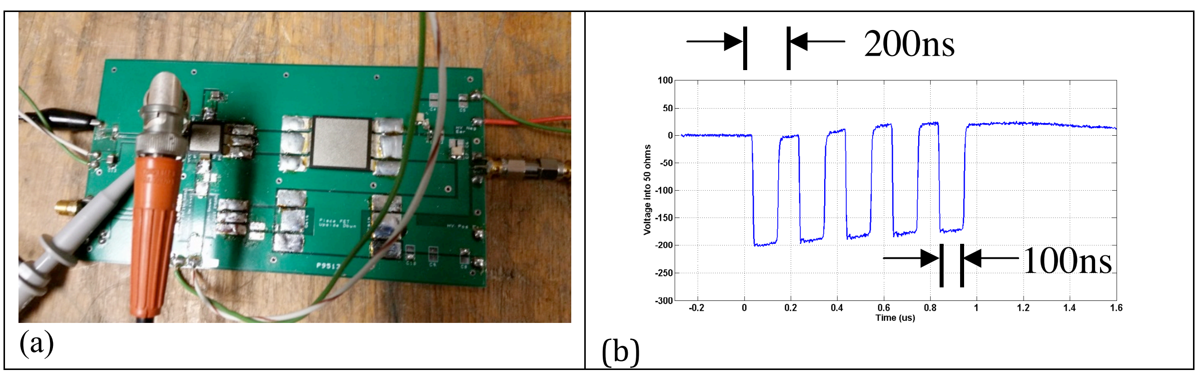

Fig. 24a-b: (a) – Prototyping RF power MOSFETs and low-side ultrafast gate drivers for a solid state grid pulser. (b) – Five pulse 200v burst at 5MHz into a 50W load with 100ns pulse widths.

A prototyping circuit (shown in Fig. 24a) is used to test the low-side driver and RF power MOSFETs from IXYS into a 50W load. The MOSFETs are capable of peak voltages of

1kV and currents of 20A switching within 5ns where the driver can handle a maximum switching frequency of 45MHz [12]. The output of the circuit is shown in Fig. 13b across a 50W resistor. We are also pursuing planar 'lighthouse' [13] tube based switching circuits as they are able to switch with sub-nanosecond rise/fall times.

Electron Sources for Prototyping

Many in-house sources have been explored as a possibility for prototyping grid drivers and resonant structures, such as the SLAC klystron gun [14] and a Varian gyro TWT gun [15]. Colleagues at NRL have a CPI-IOT gridded gun that has shown to be the most promising of the options [16]. We are in the process taking numerous measurements of their CPI-IOT gridded gun, exploring the possibility of using their gun for prototyping. Figure 25 below illustrates one of their multiple IOT guns setup for emittance measurements.

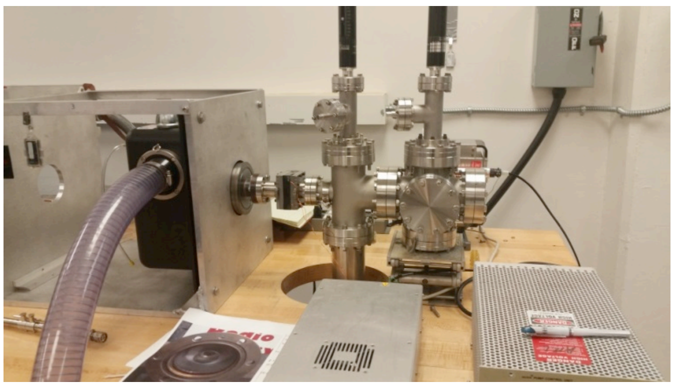

Fig. 25: NRL IOT gun setup for emittance measurements.

The input coupler that normally feeds the input RF to the gun is 'blind' to frequencies in our region of interest. An alternate means of pulsing the gun is available through the DC grid connection. A few circuit modifications to the NRL cathode pulser are required along with a fast grid pulser capable of driving the total capacitance of the surrounding circuits in parallel with the grid-to-cathode capacitance.

Plans for 2015

- The next steps for gun simulations will include optimizing the magnetic field profile for finitely permeable iron, and assembling a mechanical drawing of the proposed gun. Additionally, Michelle will be used to replicate an end to end source to collector simulation. It may be possible to model the gap voltage as a circuit element, to accurately predict the output power.

- WARP/Michelle simulations will focus on beam dynamics in the decelerating gap and consider collector designs

- The next steps for the prototype resonant structure will include exploring both input and output coupling of the structure and mechanical tunability. Then a resonant structure to be used with beam will be designed and tested that includes motorized stages to tune the resonant frequency of the capacitor gap.

- The next steps for the grid driver will include designing and constructing a complete modulator that is optically coupled to allow the driver to float up with the deck potential of the cathode.

- The next step for the NRL CPI-IOT gridded gun is to make the circuit modifications to the NRL cathode pulser to include a grid driver of the sort to be used for the MIG gun currently being designed.

References:

3. John Petillo, et al., “Recent Developments in the MICHELLE 2D/3D Electron Gun and Collector Modeling Code”, IEEE Trans. Electron Devices Sci., vol. 52, no. 5,May 2005, pp. 742-748.
4. Alex Friedman, Ronald H. Cohen, David P. Grote, Steven M. Lund, and William M. Sharp, Jean-Luc Vay, Irving Haber and Rami A. Kishek, *"Computational Methods in the Warp Code Framework for Kinetic Simulations of Particle Beams and Plasmas,"*. IEEE Transactions On Plasma Science **42(5)**, 1321 (2014).
5. J. D. Lawson, “Physics of Charged Particle Beams”, Oxford University Press, 1977.
6. R. B. Miller, “An Introduction to the Physics of Intense Charged Particle Beams”, Plenum Press, New York, 1982.
7. M. Reiser, “Theory and Design of Charged Particle Beams”, John Wiley & sons, Inc., New York, 1994, Ch. 4.
8. http://www.ansys.com/
9. R. L. Poirier, “Perpendicular Biased Ferrite-Tuned Cavities”, Proceedings of the 1993 Particle Accelerator Conference, 753 (1993).
10. http://www.ixys.com
11. http://www.tubecollectors.org/eimac/archives/7211%2864%29.pdf
12. R.F. Koontz, T.G. Lee, C. Pearson, and A.E. Vlicks, “Recent Performance, Lifetime, and Failure Modes of the 5045 Klystron Population at SLAC”, Proceedings of the 1992 Linear Accelerator Conference, 740 (1992).
13. J.N. Eckstein, D.W. Latshaw, D.S. Stone, “95GHz Gyro Traveling Wave Tube”, VARIAN, (1983).
14. S. H. Gold, A. Ting, V. Jabotinski, B Zhou, and P. Sprangle, Physical Review Special Topic – Accelerators and Beams, **16**, 083401 (2013).

Personnel supported
Students: Dymitro Kashyn, Kiersten Ruisard, Joe Hart, Amith Narayan
Faculty: Thomas Antonsen, John Rodgers, Brian Beaudoin, Gregoriy Nusinovich
Visiting Faculty: Irving Haber, Simon London
Consultant: Edward Wright

Collaboration: Steven Gold and Antonio Ting, Naval Research Laboratory

Publications: none yet

Presentations: Novel High Power Sources for the Physics of Ionospheric Modification, B. Beaudoin, T.M Antonsen Jr, I. Haber, T.W. Koeth, G. Nusinovich, K. Ruisard, J.C. Rodgers, submitted to IPAC2015.